*J. Fluid Mech.* (2010), *vol.* 645, *pp.* 411–434.  
doi:10.1017/S0022112009992709

# Interactions between steady and oscillatory convection in mushy layers

PETER GUBA[1]† AND M. GRAE WORSTER[2]

[1]Department of Applied Mathematics and Statistics, Faculty of Mathematics, Physics and Informatics, Comenius University, 842 48 Bratislava, Slovakia

[2]Institute of Theoretical Geophysics, Department of Applied Mathematics and Theoretical Physics, University of Cambridge, Wilberforce Road, Cambridge CB3 0WA, UK

(Received 4 August 2009; revised 12 October 2009; accepted 12 October 2009; first published online 4 February 2010)

We study nonlinear, two-dimensional convection in a mushy layer during solidification of a binary mixture. We consider a particular limit in which the onset of oscillatory convection just precedes the onset of steady overturning convection, at a prescribed aspect ratio of convection patterns. This asymptotic limit allows us to determine nonlinear solutions analytically. The results provide a complete description of the stability of and transitions between steady and oscillatory convection as functions of the Rayleigh number and the compositional ratio. Of particular focus are the effects of the basic-state asymmetries and non-uniformity in the permeability of the mushy layer, which give rise to abrupt (hysteretic) transitions in the system. We find that the transition between travelling and standing waves, as well as that between standing waves and steady convection, can be hysteretic. The relevance of our theoretical predictions to recent experiments on directionally solidifying mushy layers is also discussed.

## 1. Introduction

Many modern industrial processes require the production of high quality materials, many of which are produced by the directional solidification of multi-component alloys. During the solidification of an alloy, a mushy layer often forms, which is a region of partially solidified melt with a complex dendritic structure. Comprehensive reviews of previous theoretical and experimental developments on binary alloy solidification in mushy layers can be found in Worster (1997, 2000) and Davis (2001). Below, we review briefly the work relevant to the present study.

In the presence of gravity, unstable density gradients can form as a result of rejection of a lighter component of the binary mixture upon solidification, driving compositional convection in a mushy layer. The convective transport of heat and solute can modify the solid structure of the mushy layer, which, in turn, alters the fluid flow. A striking example of this mechanism is the formation of chimneys – localized channels free of solid through which buoyant fluid emanates. Chimneys are responsible for undesirable structural properties of the resultant solidified product (e.g. Copley *et al.* 1970).

A number of linear-stability analyses (Worster 1992; Emms & Fowler 1994; Anderson & Worster 1996), weakly nonlinear analyses (Amberg & Homsy 1993;

† Email address for correspondence: Peter.Guba@fmph.uniba.sk

Anderson & Worster 1995; Chung & Chen 2000; Riahi 2002, 2004; Guba & Worster 2006; Roper, Davis & Voorhees 2008) and nonlinear computations (Schulze & Worster 1998, 1999; Chung & Worster 2002) of convection in mushy layers have been carried out. Among these, the linear-stability analysis of Anderson & Worster (1996) and the weakly nonlinear analyses of Anderson & Worster (1995) and Guba & Worster (2006) are closely related to the present study.

Using a simple model introduced by Amberg & Homsy (1993), Anderson & Worster (1995) performed a weakly nonlinear-stability analysis of steady convection in a mushy layer and revealed the possibility of an oscillatory (Hopf) bifurcation. Subsequently, Anderson & Worster (1996) examined the linear stability in greater detail and indeed identified an oscillatory mode of instability. They associated this oscillatory mode with a phase lag between the background macroscopic solidification and the local dissolution caused by the fluid flow.

The nonlinear development of the oscillatory mode, identified by Anderson & Worster (1995, 1996), was considered by Guba & Worster (2006). They performed a weakly nonlinear stability analysis to resolve which of travelling or standing waves with a two-dimensional roll planform would occur near the onset of convection. They found that either wave motion could be supercritically stable, depending on the sensitivity of permeability of the mushy layer to variations in the local solid fraction. Additionally, the oscillatory solution that is stable was found to have the larger Nusselt number, and is therefore more efficient at transporting solute in the system. Building on the linear-stability results of Anderson & Worster (1996), they also examined the structure of the nonlinear oscillatory solutions and determined their signatures left behind in the resulting eutectic solid. Their analysis was focused on parameter regimes in which the oscillatory instability did not interact with the steady mode of convection. It is the nature of this nonlinear interaction which we shall elucidate here.

The possibility of oscillatory convection in mushy layers seems to have strong support in recent laboratory experiments. Solomon & Hartley (1998) performed experiments on an ammonium chloride solution in Hele-Shaw cells, cooling and solidifying the solution from a fixed base. A roughly periodic pattern of chimney convection was observed, in which the lateral locations of the chimneys remained fixed while the strength of plume convection rising from neighbouring chimneys oscillated in time out of phase with each other. This periodic behaviour is characteristic of standing-wave oscillations with flow reversals and could appear (Guba & Worster 2006) as a supercritical primary Hopf bifurcation.

Peppin, Huppert & Worster (2008) conducted laboratory experiments on aqueous solutions of ammonium chloride in a Hele-Shaw cell, in which the solutions were translated at prescribed rates through a fixed temperature gradient. By varying the experimental operating conditions, they determined a regime diagram that quantified different steady-state convection regimes as a function of the pulling speed and initial composition of the solution. Near to the boundary marking the chimney to no-chimney transition, a 'breathing mode' of chimney convection was observed, in which chimneys all periodically appeared and disappeared in phase. Such periodic behaviour might be caused by nonlinear oscillations about a steady state which do not result in a reversal of the main steady flow. Here, we include the physical effects associated with the higher-order permeability variations and interactions between the temperature and the solid structure of the mushy layer, and by doing so identify a way by which such stable vacillations can be found.

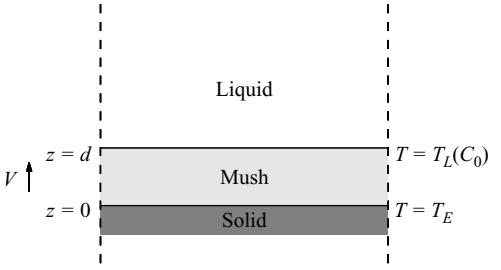


FIGURE 1. A schematic diagram of the system under consideration, showing the solid, mush and liquid. The system is continuously being solidified at speed $V$ in the vertical direction. The mushy layer is assumed to have constant thickness $d$. The bottom boundary $z = 0$ of the mushy layer is kept at the eutectic temperature $T_E$, and the top boundary $z = d$ at the liquidus temperature $T_L(C_0)$. The top and bottom boundaries of the mushy layer are taken to be rigid, impermeable and isothermal. Mixture with concentration $C_0$ is fed into the mushy layer through the mush–liquid interface.

In addition to the nonlinear-stability properties of steady and oscillatory convecting states alone (Anderson & Worster 1995; Guba & Worster 2006), one is naturally interested in the nature of the possible transitions between the steady and oscillatory solutions that occur as the system control parameters are varied. In the present paper, a problem of this sort is analysed by studying the mushy-layer system in the vicinity of a particular multiple bifurcation associated with the coalescence of the steady-state and oscillatory bifurcations. The analysis provides a complete description of the nonlinear interactions between the steady and oscillatory states and predicts hysteretic transitions in the system. Some of the predictions are interpreted in terms of experimentally relevant dimensional control parameters.

The paper is organized as follows. In § 2, we formulate the problem. In § 3, we perform a two-time scale asymptotic analysis to derive an amplitude equation that describes the nonlinear coupling between the steady and oscillatory states. In § 4, we analyse the amplitude equation and make predictions of nonlinear stability. We identify conditions under which the mushy-layer system exhibits hysteretic transitions between convecting states. Finally, in § 5 we give some conclusions.

## 2. Formulation

Formulation of the problem follows that given in Anderson & Worster (1995), and later used by Guba & Worster (2006). For completeness, the main aspects of the formulation are also described here.

The physical system under consideration consists of a horizontal mushy layer lying between a completely solid region below and a completely liquid region above, as illustrated in figure 1. The system is cooled uniformly from below such that the solid–mush and mush–liquid interfaces advance upwards with a constant solidification speed $V$. We adopt a simplification that the mushy layer is dynamically isolated from the rest of the system (Amberg & Homsy 1993) by assuming the top and bottom boundaries of the mushy layer to be non-deformable, impermeable to fluid flow and isothermal. The system is studied in a frame of reference moving upwards with velocity $V$ relative to the solid formed at the bottom of the mushy layer and

the solid dendrites within the mushy layer, allowing the non-convecting basic state to be steady. In this frame of reference, the bottom boundary of the mushy layer $z = 0$ is kept at the eutectic temperature $T = T_E$, while the top boundary $z = d$ is kept at the liquidus temperature $T_L(C_0)$ and is a surface through which the mixture of composition $C_0$ is supplied.

The temperature $T$ and the composition $C$ of the liquid in the mushy layer are required to satisfy a linear liquidus relationship

$$T = T_L(C) \equiv T_L(C_0) + \Gamma(C - C_0), \tag{2.1}$$

where $\Gamma$ is a constant. The liquid is assumed to be Newtonian with a linearized equation of state

$$\rho_l = \rho_0[1 + \beta(C - C_0)], \tag{2.2}$$

where $\rho_0$ is a reference density, $\beta = \beta^* - \alpha^*\Gamma$, and $\alpha^*$ and $\beta^*$ are the constant expansion coefficients for heat and solute, respectively.

We begin with the dimensionless equations describing conservation of heat, solute, momentum and mass in the reference frame translating with the eutectic front (see e.g. Worster 1992) given by

$$\left(\frac{\partial}{\partial t} - \frac{\partial}{\partial z}\right)(\theta - S\phi) + \boldsymbol{u}\cdot\nabla\theta = \nabla^2\theta, \tag{2.3a}$$

$$\left(\frac{\partial}{\partial t} - \frac{\partial}{\partial z}\right)[(1-\phi)\theta + \mathscr{C}\phi] + \boldsymbol{u}\cdot\nabla\theta = 0, \tag{2.3b}$$

$$K(\phi)\boldsymbol{u} = -\nabla p - Ra\,\theta\hat{\boldsymbol{z}}, \tag{2.3c}$$

$$\nabla\cdot\boldsymbol{u} = 0, \tag{2.3d}$$

where the dependent variables are the temperature (or equivalently composition) $\theta$, the local solid fraction $\phi$, the Darcy fluid velocity $\boldsymbol{u}$ and the pressure $p$. The governing equations have been made dimensionless by scaling the temperature difference $T - T_L(C_0)$ with $\Delta T = \Gamma\Delta C = T_L(C_0) - T_E$, where $\Delta C = C_0 - C_E$ and $C_E$ is the eutectic composition; velocity with $V$; length and time with the thermal-diffusion length scale and time scale $\kappa/V$ and $\kappa/V^2$; and pressure with $\kappa\mu/\Pi(0)$, where $\mu$ is the dynamic viscosity of the liquid and $\Pi(0)$ is the reference permeability of the layer. The function $K(\phi)$ defined by $K(\phi) = \Pi(0)/\Pi(\phi)$ accounts for the variations of permeability $\Pi$ with the local solid fraction $\phi$; see (2.12).

The mushy-layer system is controlled by the three dimensionless parameters $S$, $\mathscr{C}$ and $Ra$ defined by

$$S = \frac{L}{c_l\Delta T}, \quad \mathscr{C} = \frac{C_S - C_0}{C_0 - C_E}, \quad Ra = \frac{\rho_0\beta\Delta C g\Pi(0)}{\mu V}. \tag{2.4a–c}$$

These quantities are respectively the Stefan number, the compositional ratio and the Rayleigh number. Here, $L$ is the latent heat of solidification, $c_l$ is the specific heat, $C_S$ is the composition of solid forming the dendrites and $g$ is the gravitational acceleration.

We adopt the simple boundary conditions

$$\theta = -1, \quad w = 0 \quad \text{on} \quad z = 0, \tag{2.5a,b}$$

$$\theta = 0, \quad w = 0, \quad \phi = 0 \quad \text{on} \quad z = \delta, \tag{2.5c–e}$$

where $\delta$ is a measure of the dimensionless height of the mushy layer defined as $\delta = d/(\kappa/V)$ and $w$ is the $z$-component of $\boldsymbol{u}$. For a detailed discussion of these conditions, the reader is referred to Anderson & Worster (1995).

We proceed by reducing the model asymptotically. First, following Amberg & Homsy (1993), we study a limit in which the thickness of the mushy layer is much less than the diffusion length scale by letting $\delta \ll 1$. Secondly, we assume that the compositional ratio is large by writing

$$\mathscr{C} = \bar{\mathscr{C}}/\delta, \quad \text{with} \quad \bar{\mathscr{C}} = O(1) \quad \text{as} \quad \delta \to 0, \tag{2.6}$$

which corresponds to the near-eutectic approximation introduced by Fowler (1985). Thirdly, we consider the limit in which the Stefan number is large (Emms & Fowler 1994) by taking

$$S = \bar{S}/\delta, \quad \text{with} \quad \bar{S} = O(1) \quad \text{as} \quad \delta \to 0, \tag{2.7}$$

which corresponds to the situation in which the latent heat liberated during the local phase change is much larger than the heat associated with the typical variations of temperature across the mushy layer. Note that this particular scaling allows the destabilization of the system to an oscillatory mode of convection (Anderson & Worster 1995; Guba & Worster 2006).

An analysis of the balances in (2.3) for these asymptotic limits then indicates the following rescalings of the problem:

$$(x, z) = \delta(\bar{x}, \bar{z}), \quad t = \delta^2 \bar{t}, \quad R^2 = \delta Ra, \tag{2.8a–c}$$

$$\theta = \theta_B(\bar{z}) + \epsilon\hat{\theta}(\bar{x}, \bar{z}, \bar{t}), \tag{2.8d}$$

$$\phi = \phi_B(\bar{z}) + \epsilon\hat{\phi}(\bar{x}, \bar{z}, \bar{t}), \tag{2.8e}$$

$$\boldsymbol{u} = \boldsymbol{0} + \epsilon\frac{R}{\delta}\hat{\boldsymbol{u}}(\bar{x}, \bar{z}, \bar{t}), \tag{2.8f}$$

$$p = Rp_B(\bar{z}) + \epsilon R\hat{p}(\bar{x}, \bar{z}, \bar{t}), \tag{2.8g}$$

where the subscript $B$ denotes a non-convecting basic state, in the moving frame, which is perturbed by the small convective disturbances measured by a perturbation amplitude $\epsilon$. Note that the basic state is steady and horizontally uniform, while the two-dimensional disturbances can vary in the vertical and horizontal directions and in time.

The approximate basic-state solutions to the problem, resulting from (2.3) and (2.5), under the particular asymptotic limits given by (2.6) and (2.7) can be obtained as series expansions in powers of $\delta$, yielding

$$\theta_B = -(1 - \bar{z}) + \delta\frac{\Omega}{2}\bar{z}(1 - \bar{z}) + O(\delta^2), \tag{2.9a}$$

$$\phi_B \equiv \delta\bar{\phi}_B = \delta\frac{1}{\bar{\mathscr{C}}}(1 - \bar{z}) - \delta^2\left(\frac{1}{\bar{\mathscr{C}}^2}(1 - \bar{z})^2 + \frac{\Omega}{2\bar{\mathscr{C}}}\bar{z}(1 - \bar{z})\right) + O(\delta^3), \tag{2.9b}$$

where the $O(1)$ parameter $\Omega = 1 + \bar{S}/\bar{\mathscr{C}}$ represents a measure of the coupling between the thermal and solid-fraction fields. Note that $\phi_B$ is vanishing and $\theta_B$ is linear in the limit $\delta \to 0$, the results directly related to the onset of convection in a non-reacting porous layer as studied by Palm, Weber & Kvernvold (1972). It is the higher-order terms in $\delta$ that are associated with effects pertinent to the mushy layer.

The equations governing convective, in general nonlinear, perturbations are

$$\left(\frac{\partial}{\partial \bar{t}} - \delta\frac{\partial}{\partial \bar{z}}\right)\left(\hat{\theta} - \frac{\bar{S}}{\delta}\hat{\phi}\right) + R\hat{w}\frac{\mathrm{d}\theta_B}{\mathrm{d}\bar{z}} - \nabla^2\hat{\theta} = -\epsilon R\hat{\boldsymbol{u}}\cdot\nabla\hat{\theta}, \quad (2.10a)$$

$$\left(\frac{\partial}{\partial \bar{t}} - \delta\frac{\partial}{\partial \bar{z}}\right)\left((1-\delta\bar{\phi}_B)\hat{\theta} - \theta_B\hat{\phi} - \epsilon\hat{\theta}\hat{\phi} + \frac{\bar{\mathscr{C}}}{\delta}\hat{\phi}\right) + R\hat{w}\frac{\mathrm{d}\theta_B}{\mathrm{d}\bar{z}} = -\epsilon R\hat{\boldsymbol{u}}\cdot\nabla\hat{\theta}, \quad (2.10b)$$

$$\nabla^2[K(\delta\bar{\phi}_B + \epsilon\hat{\phi})\hat{u}] - \frac{\partial}{\partial \bar{x}}[\hat{\boldsymbol{u}}\cdot\nabla K(\delta\bar{\phi}_B + \epsilon\hat{\phi})] - R\frac{\partial^2\hat{\theta}}{\partial\bar{x}\partial\bar{z}} = 0, \quad (2.10c)$$

$$\nabla^2[K(\delta\bar{\phi}_B + \epsilon\hat{\phi})\hat{w}] - \frac{\partial}{\partial \bar{z}}[\hat{\boldsymbol{u}}\cdot\nabla K(\delta\bar{\phi}_B + \epsilon\hat{\phi})] + R\frac{\partial^2\hat{\theta}}{\partial\bar{x}^2} = 0, \quad (2.10d)$$

with the boundary conditions

$$\hat{\theta} = 0, \quad \hat{w} = 0 \quad \text{on} \quad \bar{z} = 0, \quad (2.11a,b)$$

$$\hat{\theta} = 0, \quad \hat{w} = 0, \quad \hat{\phi} = 0 \quad \text{on} \quad \bar{z} = 1. \quad (2.11c\text{–}e)$$

An important feature of the dynamics of the mushy layer is the variation of the permeability with the local solid fraction. Here, since the basic-state solid fraction is small, of $O(\delta)$, and the perturbation to the solid fraction is also expected to be small in the context of the weakly nonlinear theory to be developed, we expand the function $K(\phi)$ in a regular series for $\phi \ll 1$

$$K(\phi) = 1 + K_1\phi + K_2\phi^2 + O(\phi^3), \quad (2.12)$$

where $K_1$ and $K_2$ are constants specifying a particular form of the constitutive relationship. Note that $K_1$ must be positive in order to ensure the decreasing of the permeability $\Pi(\phi)$ with increasing solid fraction $\phi$. In what follows, we shall consider a particular limiting case in which $K_1$ is small by taking

$$K_1 = \delta\bar{K}_1, \quad \text{with} \quad \bar{K}_1 = O(1) \quad \text{as} \quad \delta \to 0. \quad (2.13)$$

## 3. The Takens–Bogdanov bifurcation

The analysis we shall pursue has the following three steps. The first step involves the identification of the critical parameter values for which steady and oscillatory convection in the mushy layer set in simultaneously (§ 3.1). The second step pertains to the derivation of an amplitude equation describing the dynamics near this multiple bifurcation (§ 3.2). Formal procedures for systematic derivation of such an equation have been described in detail in the literature on competing instabilities (e.g. Knobloch & Proctor 1981; Coullet & Spiegel 1983; Guckenheimer & Knobloch 1983). Here we shall use a complex-extended version of the perturbation procedure devised by Spiegel (1994). The third step then involves the analysis of the amplitude equation to make specific predictions for the mushy-layer system in terms of transitions between, and stability of, the steady and oscillatory convection patterns (§ 4).

### 3.1. *Linear-stability problem: summary*

To motivate our approach at the nonlinear stage, we commence by reviewing the results of the linear-stability problem for (2.10) and (2.11). Linear-stability theory (Anderson & Worster 1996) shows that, in the limit $\delta \to 0$, the onset of a neutral

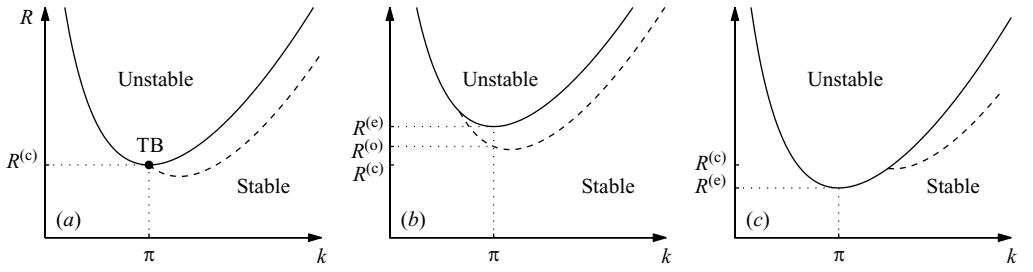


FIGURE 2. Neutral stability curves in the $(k, R)$-plane sketched for three cases: $(a)$ $\bar{\mathscr{C}} = \bar{\mathscr{C}}^{(c)}$, $(b)$ $\bar{\mathscr{C}} < \bar{\mathscr{C}}^{(c)}$ and $(c)$ $\bar{\mathscr{C}} > \bar{\mathscr{C}}^{(c)}$. The solid (dashed) curve corresponds to the steady (oscillatory) instability branch. The system is linearly stable (unstable) below (above) each curve. The two stability curves intersect at a Takens–Bogdanov point where the two modes bifurcate from the basic state simultaneously at a single wavenumber and the frequency vanishes. In $(a)$, this point, labelled TB, coincides with the minimum of the steady branch at $k = \pi$. Note that the minimum of the oscillatory branch is separated from TB by $O(\delta)$ in both $k$ and $R$. At $k = \pi$, fixed throughout the analysis, the bifurcation from the basic state of oscillatory mode precedes that of steady mode in $(b)$, while the oscillatory mode is absent in $(c)$. The nonlinear modal interactions near TB of $(a)$ are described in § 3.

steady mode occurs at $R = R^{(e)} \equiv \Omega^{-1/2}\left[R_{00} + \delta R_{01}^{(e)} + O(\delta^2)\right]$, where

$$R_{00} = \frac{\pi^2 + k^2}{k}, \tag{3.1a}$$

$$R_{01}^{(e)} = R_{00}\left(\frac{1}{4} + \frac{2}{\pi^2}\right)\frac{\bar{S}}{\Omega\bar{\mathscr{C}}^2} \tag{3.1b}$$

and $k$ is the horizontal wavenumber of the perturbation. The steady stability curve attains its minimum value at $k = \pi$. The onset of a neutral oscillatory mode with a linear oscillation frequency $\omega = \delta\omega_{01} + O(\delta^2)$ occurs at $R = R^{(o)} \equiv \Omega^{-1/2}\left[R_{00} + \delta R_{01}^{(o)} + O(\delta^2)\right]$, where

$$R_{01}^{(o)} = R_{00}\left[\frac{1}{4} + \frac{\pi^2(1 + \cos\omega_{01})}{(\pi^2 - \omega_{01}^2)^2}\right]\frac{\bar{S}}{\Omega\bar{\mathscr{C}}^2} \tag{3.2a}$$

and $\omega_{01}$ satisfies

$$0 = \omega_{01}\left[1 + \frac{\pi^2 + k^2}{\pi^2 - \omega_{01}^2}\left(1 - \frac{2\pi^2}{\pi^2 - \omega_{01}^2}\frac{\sin\omega_{01}}{\omega_{01}}\right)\frac{\bar{S}}{\Omega^2\bar{\mathscr{C}}^2}\right]. \tag{3.2b}$$

An account of the parametric dependence of the oscillatory mode, determined from (3.2*a*,*b*), is given by Anderson & Worster (1996). Their numerical results indicate that the minimizing wavenumber for the oscillatory mode varies with the parameters $\bar{S}$, $\bar{\mathscr{C}}$ and $\delta$, and is always greater than that for the steady mode (see also figure 5 of Guba & Worster 2006).

The salient features of the linear-stability analysis are summarized in figures 2 and 3. Figure 2 shows the neutral stability curves for the steady and oscillatory modes for representative values of $\bar{\mathscr{C}}$ at fixed $\bar{S}$ and $\delta$. The two stability curves intersect at a codimension-two point of the Takens–Bogdanov type, where the two modes bifurcate from the basic state simultaneously at a single wavenumber and the oscillatory frequency vanishes. Focusing, for simplicity, on the wavenumber $k = \pi$, we deduce, from (3.1*b*) and (3.2*a*,*b*), that this occurs at the critical values $R = R^{(c)}$ and

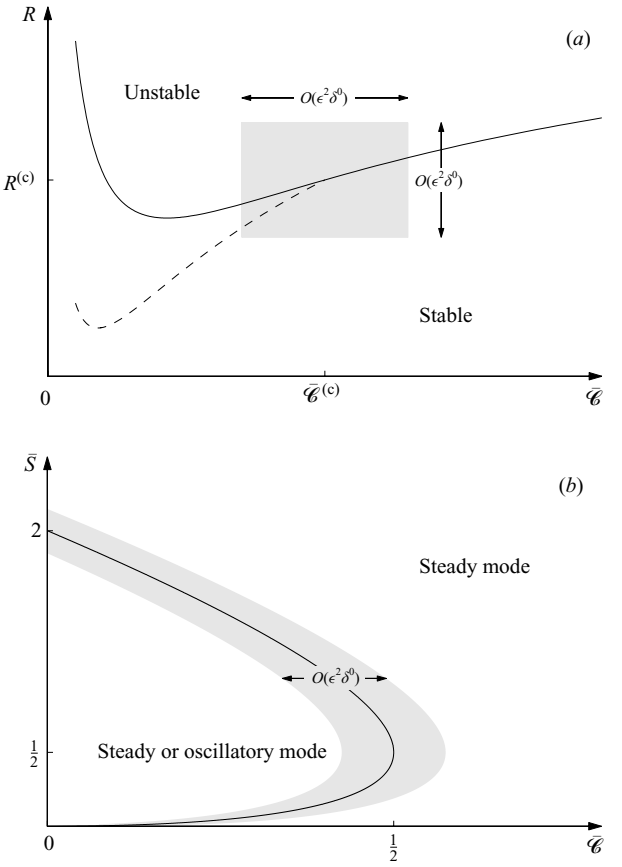


FIGURE 3. (*a*) Linear-stability boundaries in the $(\bar{\mathscr{C}}, R)$-plane sketched for $k = \pi$ and fixed $\bar{S}$ and $\delta$. The solid (dashed) curve corresponds to the steady (oscillatory) mode of instability. The system is stable (unstable) below (above) each curve. The curves meet at the point $\left(\bar{\mathscr{C}}^{(c)}, R^{(c)}\right)$. The oscillatory mode exists when $\bar{\mathscr{C}} \leqslant \bar{\mathscr{C}}^{(c)}$, and is always less stable than the steady mode. (*b*) Linear regime diagram in the $(\bar{\mathscr{C}}, \bar{S})$-plane sketched for $k = \pi$. The steady mode is possible for any parameter values, while the oscillatory mode exists within the region bounded by a curve defined by $\bar{\mathscr{C}} = \bar{\mathscr{C}}^{(c)}(\bar{S})$. The asymptotic analysis of § 3 is valid in the shaded regions.

$\bar{\mathscr{C}} = \bar{\mathscr{C}}^{(c)}$ given by

$$\begin{aligned} \Omega^{(c)1/2} R^{(c)} &\equiv R_{00}^{(c)} + \delta R_{01}^{(c)} + O(\delta^2) \\ &= 2\pi + \delta \left( \frac{4}{\pi} + \frac{\pi}{2} \right) \frac{\bar{S}}{\Omega_{00}^{(c)} \bar{\mathscr{C}}_{00}^{(c)2}} + O(\delta^2), \qquad (3.3a) \\ \bar{\mathscr{C}}^{(c)} &\equiv \bar{\mathscr{C}}_{00}^{(c)} + O(\delta) \\ &= \sqrt{2}\bar{S}^{1/2} - \bar{S} + O(\delta), \qquad (3.3b) \end{aligned}$$

provided $\bar{S} \leqslant 2$, where $\Omega^{(c)} = 1 + \bar{S}/\bar{\mathscr{C}}^{(c)}$ and $\Omega_{00}^{(c)} = 1 + \bar{S}/\bar{\mathscr{C}}_{00}^{(c)}$. The $O(\delta)$ correction term to $\bar{\mathscr{C}}_{00}^{(c)}$ in (3.3*b*) can be determined by proceeding to higher order (see § 3.2). At this special Takens–Bogdanov point, the oscillatory mode terminates on the steady mode at the minimum of the steady stability curve (figure 2*a*). Figure 3(*a*) illustrates the Rayleigh numbers for the steady and oscillatory modes as functions of $\bar{\mathscr{C}}$ for

$k = \pi$ at fixed $\bar{S}$ and $\delta$, while figure 3($b$) shows the path of Takens–Bogdanov points in the $(\bar{\mathscr{C}}, \bar{S})$-plane as given by (3.3$b$). The results of figures 2 and 3 suggest that the compositional ratio $\bar{\mathscr{C}}$ can be used to adjust the onset of oscillatory instability. We exploit this tuning behaviour in the subsequent nonlinear analysis.

### 3.2. *Derivation of the amplitude equation*

A branch of steady solutions bifurcates from $R^{(\mathrm{e})}$, while a branch of oscillatory solutions bifurcates from $R^{(\mathrm{o})}$. The nonlinear solutions in the neighbourhood of these simple bifurcations are now well understood (see Amberg & Homsy 1993 and Anderson & Worster 1995 for steady solutions; Guba & Worster 2006 for oscillatory solutions). Here, we are interested in studying the nonlinear solutions in the neighbourhood of the multiple bifurcation defined by (3.3). Hence, we write

$$\Omega^{1/2} R = R_{00}^{(\mathrm{c})} + \delta R_{01}^{(\mathrm{c})} + \cdots + \epsilon(R_{10} + \delta R_{11} + \cdots) + \epsilon^2(R_{20} + \delta R_{21} + \cdots) + \cdots, \quad (3.4a)$$

$$\bar{\mathscr{C}} = \bar{\mathscr{C}}_{00}^{(\mathrm{c})} + \delta \bar{\mathscr{C}}_{01}^{(\mathrm{c})} + \cdots + \epsilon(\bar{\mathscr{C}}_{10} + \delta \bar{\mathscr{C}}_{11} + \cdots) + \epsilon^2(\bar{\mathscr{C}}_{20} + \delta \bar{\mathscr{C}}_{21} + \cdots) + \cdots. \quad (3.4b)$$

Note that it would be equivalent, but mathematically less convenient, to expand $\bar{S}$ instead of $\bar{\mathscr{C}}$. Similarly, we expand the perturbation quantities in the forms

$$\hat{\theta} = (\theta_{00} + \delta\theta_{01} + \cdots) + \epsilon(\theta_{10} + \delta\theta_{11} + \cdots) + \epsilon^2(\theta_{20} + \delta\theta_{21} + \cdots) + \epsilon^3(\theta_{30} + \delta\theta_{31} + \cdots) + \cdots, \quad (3.5a)$$

$$\Omega\hat{\phi} = (\phi_{00} + \delta\phi_{01} + \cdots) + \epsilon(\phi_{10} + \delta\phi_{11} + \cdots) + \epsilon^2(\delta^{-1}\phi_{2(-1)} + \phi_{20} + \delta\phi_{21} + \cdots) + \epsilon^3(\delta^{-1}\phi_{3(-1)} + \phi_{30} + \delta\phi_{31} + \cdots) + \cdots, \quad (3.5b)$$

$$\Omega^{1/2}\hat{\boldsymbol{u}} = (\boldsymbol{u}_{00} + \delta\boldsymbol{u}_{01} + \cdots) + \epsilon(\boldsymbol{u}_{10} + \delta\boldsymbol{u}_{11} + \cdots) + \epsilon^2(\boldsymbol{u}_{20} + \delta\boldsymbol{u}_{21} + \cdots) + \epsilon^3(\boldsymbol{u}_{30} + \delta\boldsymbol{u}_{31} + \cdots) + \cdots. \quad (3.5c)$$

Here, we assume that $0 \leqslant \epsilon \ll \delta \ll 1$. Note the appearance of singular terms in the expansion for $\hat{\phi}$ at $O(\epsilon^2)$ and $O(\epsilon^3)$ as $\delta \to 0$. However, since we consider the double limit where $\delta = O(1)$ as $\epsilon \to 0$, the asymptotic representation (3.5$b$) is, in fact, well defined. These terms are discussed further below.

As $\epsilon \to 0$ with $\delta$ kept fixed, $R$ is close to both $R^{(\mathrm{e})}$ and $R^{(\mathrm{o})}$, and the oscillation frequency $\omega$ is small. Specifically, from (3.2$b$) we find

$$\omega \sim \epsilon\delta \left[ -\frac{6\pi^2}{\pi^2 - 9} \frac{1}{\Omega_{00}^{(\mathrm{c})}} \frac{\bar{\mathscr{C}}_{20}}{\bar{\mathscr{C}}_{00}^{(\mathrm{c})}} \right]^{1/2}, \quad (3.6)$$

provided $\bar{\mathscr{C}}_{20} < 0$ (and in anticipation of vanishing $O(\epsilon)$ terms in (3.4$b$) for two-dimensional convection; see below). There are two distinct time scales in the problem: an $O(\epsilon\delta)$ oscillatory time scale suggested by linear theory, and a slow $O(\epsilon^2)$ time scale on which thermal dissipation and forcing act. Thus, we define

$$\tilde{t} = \epsilon\delta\bar{t} \quad \text{and} \quad \hat{t} = \epsilon^2\bar{t}, \quad (3.7a,b)$$

so that $\partial/\partial\bar{t} \mapsto \epsilon\delta\partial/\partial\tilde{t} + \epsilon^2\partial/\partial\hat{t}$.

Substituting (3.4) and (3.5) into a rescaled version of (2.10) and (2.11), we obtain a system that can be solved sequentially. At $O(\epsilon^0\delta^0)$, we recover the leading-order

linear stability problem at the codimension-two point. The solutions take the form

$$\theta_{00} = -\sin(\pi\bar{z})\eta_{00}(\bar{x},\tilde{t},\hat{t}) + \text{c.c.}, \tag{3.8a}$$

$$\phi_{00} = -\frac{2\pi}{\bar{\mathscr{C}}_{00}^{(c)}}[1+\cos(\pi\bar{z})]\eta_{00}(\bar{x},\tilde{t},\hat{t}) + \text{c.c.}, \tag{3.8b}$$

$$u_{00} = \cos(\pi\bar{z})\frac{\partial\eta_{00}(\bar{x},\tilde{t},\hat{t})}{\partial\bar{x}} + \text{c.c.}, \tag{3.8c}$$

$$w_{00} = \pi\sin(\pi\bar{z})\eta_{00}(\bar{x},\tilde{t},\hat{t}) + \text{c.c.}, \tag{3.8d}$$

$$R_{00} = R_{00}^{(c)}, \tag{3.8e}$$

where the one-dimensional planform function that describes rolls is

$$\eta_{00}(\bar{x},\tilde{t},\hat{t}) = A_{00}(\tilde{t},\hat{t})\mathrm{e}^{\mathrm{i}\pi\bar{x}}. \tag{3.9}$$

Here $A_{00}(\tilde{t},\hat{t})$ is a complex amplitude which is as yet arbitrary.

At $O(\epsilon^0\delta^1)$, we obtain the first correction terms to the linear-stability problem at the codimension-two point. The solvability condition at this order is automatically satisfied because of the definition of $R_{01}^{(c)}$ and $\bar{\mathscr{C}}_{00}^{(c)}$. The solutions take rather complicated forms and hence are not recorded here. We only note that these involve a similar planform

$$\eta_{01}(\bar{x},\tilde{t},\hat{t}) = A_{01}(\tilde{t},\hat{t})\mathrm{e}^{\mathrm{i}\pi\bar{x}}, \tag{3.10}$$

where $A_{01}(\tilde{t},\hat{t})$ is as yet arbitrary, giving rise to the amplitude function of interest defined as $\mathscr{A}_0 = A_{00} + \delta A_{01}$.

At $O(\epsilon^1\delta^0)$ and $O(\epsilon^1\delta^1)$, the existence of solutions requires

$$R_{10} = 0 \quad \text{and} \quad R_{11} = 0, \quad \bar{\mathscr{C}}_{10} = 0, \tag{3.11a–c}$$

respectively, as expected for the roll convection pattern. Again, to save space, the explicit form for the solutions at these orders is omitted, except to note that these involve two further planforms

$$\eta_{10}(\bar{x},\tilde{t},\hat{t}) = A_{10}(\tilde{t},\hat{t})\mathrm{e}^{\mathrm{i}\pi\bar{x}}, \quad \eta_{11}(\bar{x},\tilde{t},\hat{t}) = A_{11}(\tilde{t},\hat{t})\mathrm{e}^{\mathrm{i}\pi\bar{x}}, \tag{3.12a,b}$$

giving rise to the amplitude function $\mathscr{A}_1 = A_{10} + \delta A_{11}$.

At the next order, $O(\epsilon^2\delta^{-1})$, from the solute balance (2.10$b$) we have

$$-\bar{\mathscr{C}}_{00}^{(c)}\frac{\partial\phi_{2(-1)}}{\partial\bar{z}} = -\bar{\mathscr{C}}_{00}^{(c)}\frac{\partial\phi_{00}}{\partial\hat{t}}. \tag{3.13}$$

It may be noted that the solid-fraction perturbation $\phi_{2(-1)}$ appears here as a dynamic variable, instead of being slaved to the leading-order solid fraction field. This is a consequence of the slow time scale $\hat{t}$ associated with the perturbation growth rate, as noted also by Anderson & Worster (1995).

Next, we discuss the $O(\epsilon^2)$ problem, correct to $O(\delta^1)$. The solvability conditions found at $O(\epsilon^2\delta^0)$ and $O(\epsilon^2\delta^1)$ can be combined to yield the evolution equation

$$a\mathscr{A}_{0\tilde{t}\tilde{t}} - (b + c|\mathscr{A}_0|^2)\mathscr{A}_0 = 0 \tag{3.14}$$

for the amplitude $\mathscr{A}_0$, where the coefficients $a$, $b$ and $c$ are given below. We note that the $A_{00\hat{t}}$ term in the $O(\epsilon^2\delta^1)$ solvability condition has been made to vanish, determining $\bar{\mathscr{C}}_{01}^{(c)}$ as given by (A 3). In passing, we remark that (3.14) is a nonlinear conservative equation, with periodic solutions that are unstable. To recover the 'dissipation' associated with the physical effects inherent to the mushy layer, we need to proceed to higher order in $\epsilon$. We shall discuss these effects further in § 4.

As at $O(\epsilon^2)$, we find that the $O(\epsilon^3)$ problem is forced by an $O(1/\delta)$ term. Specifically, at $O(\epsilon^3\delta^{-1})$, (2.10*b*) becomes

$$-\bar{\mathscr{C}}_{00}^{(c)}\frac{\partial\phi_{3(-1)}}{\partial\bar{z}} = -\bar{\mathscr{C}}_{00}^{(c)}\frac{\partial\phi_{10}}{\partial\hat{t}} - \bar{\mathscr{C}}_{00}^{(c)}\frac{\partial\phi_{2(-1)}}{\partial\tilde{t}}. \tag{3.15}$$

Note that the variations over the two time scales $\tilde{t}$ and $\hat{t}$ come in to provide forcing for the solid-fraction perturbation $\phi_{3(-1)}$. In fact, this is the reason for the appearance of $O(1/\delta)$ term in (3.5*b*).

Applying the solvability condition at $O(\epsilon^3\delta^0)$ and $O(\epsilon^3\delta^1)$ we obtain, after some manipulation and use of (3.14), the evolution equation

$$a\mathscr{A}_{1\tilde{t}\tilde{t}} - b\mathscr{A}_1 - c\mathscr{A}_0^2\mathscr{A}_1^* - 2c|\mathscr{A}_0|^2\mathscr{A}_1 - d\mathscr{A}_{0\tilde{t}} - e\mathscr{A}_0^2\mathscr{A}_{0\tilde{t}}^* - (e+f)|\mathscr{A}_0|^2\mathscr{A}_{0\tilde{t}} + 2\bar{a}\mathscr{A}_{0\tilde{t}\hat{t}} = 0 \tag{3.16}$$

for the amplitude $\mathscr{A}_1$, where the coefficients $\bar{a}$, $d$, $e$ and $f$ are given below. We note that the term $A_{00}^2A_{00}^*$ in the $O(\epsilon^3\delta^1)$ solvability condition has been made to vanish by taking $\bar{\mathscr{C}}_{11} = 0$.

Finally, we can reconstitute (3.14) and (3.16) to obtain a *single* evolution equation

$$a\ddot{\mathscr{A}} - \left(b + c|\mathscr{A}|^2\right)\mathscr{A} - \epsilon\left[d\dot{\mathscr{A}} + e\left(\mathscr{A}^*\dot{\mathscr{A}} + \mathscr{A}\dot{\mathscr{A}}^*\right)\mathscr{A} + f|\mathscr{A}|^2\dot{\mathscr{A}}\right] = 0, \tag{3.17}$$

where

$$a \equiv \delta\bar{a} = \delta\left(1 - \frac{8}{\pi^2}\right)\Omega_{00}^{(c)} + \delta^2\bar{a}_1, \tag{3.18a}$$

$$b = 2\pi R_{20} + \delta b_1, \tag{3.18b}$$

$$c = -2\pi^4\left(1 + 11\frac{K_2}{\Omega_{00}^{(c)2}\bar{\mathscr{C}}_{00}^{(c)2}}\right) + \delta c_1, \tag{3.18c}$$

$$d = \frac{2\pi(\pi^2-9)}{3(\pi^2-8)}R_{20} + \delta d_1, \tag{3.18d}$$

$$e = -\frac{2\pi^4(\pi^2-9)}{3(\pi^2-8)}\left(1 - \frac{\pi^2+3}{\pi^2-9}\frac{K_2}{\Omega_{00}^{(c)2}\bar{\mathscr{C}}_{00}^{(c)2}}\right) + \delta e_1, \tag{3.18e}$$

$$f = -\frac{2\pi^4(\pi^2-9)}{3(\pi^2-8)}\left(1 + \frac{33\pi^4 - 169\pi^2 - 1024}{3\pi^2(\pi^2-9)}\frac{K_2}{\Omega_{00}^{(c)2}\bar{\mathscr{C}}_{00}^{(c)2}}\right) + \delta f_1. \tag{3.18f}$$

This equation determines the dynamics of the total amplitude $\mathscr{A}$ defined as $\mathscr{A} = \mathscr{A}_0 + \epsilon\mathscr{A}_1$. Here the dot represents a new, resummed derivative $\mathrm{d}/\mathrm{d}\tau = \partial/\partial\tilde{t} + (\epsilon/\delta)\partial/\partial\hat{t}$, and the asterisk denotes complex conjugation. Expressions for $\bar{a}_1$, $b_1$, $c_1$, $d_1$, $e_1$ and $f_1$ are given in the Appendix. Such an equation arises in a number of other physical systems with competing instabilities, including double-diffusive convection (Knobloch 1986), rotating Boussinesq convection (Knobloch & Silber 1990) and magnetoconvection (Dangelmayr & Knobloch 1986; Rucklidge *et al.* 1993), and its dynamics are well understood (Dangelmayr & Knobloch 1987). The form of this equation can be established on the basis of symmetry and group-theoretic arguments, while the coefficients appearing in this equation are specific to the underlying physical system. We point out here that $b$ and $d$ are linearly related to $R_{20}$, $R_{21}$ and $\mathscr{C}_{20}$, while $a$, $c$, $e$ and $f$ are particular functions of the system control parameters $\bar{S}$, $\bar{K}_1$, $K_2$ and $K_3$.

## 4. Analysis of the amplitude equation

We outline the main features of the dynamics of (3.17) in § 4.1, and exemplify the predictions for the mushy-layer system in terms of bifurcation diagrams in § 4.2 and stability maps in § 4.3.

### 4.1. *Steady and oscillatory solutions*

The amplitude equation (3.17) admits steady-state solutions ($\mathscr{A}$ real, constant), as well as oscillatory solutions in the form of travelling waves ($\mathscr{A} = |\mathscr{A}|\mathrm{e}^{\mathrm{i}\phi_{\mathscr{A}}}$ with $|\mathscr{A}|$ constant, $\dot{\phi}_{\mathscr{A}}$ constant), standing waves ($\mathscr{A}$ real, periodic) and modulated waves ($\mathscr{A} = \bar{\mathscr{A}}\mathrm{e}^{\mathrm{i}\phi_{\mathscr{A}}}$ with $\bar{\mathscr{A}}$ periodic, $\dot{\phi}_{\mathscr{A}}$ constant). The steady states are given by

$$\mathscr{A}^2 = -b/c \tag{4.1}$$

and arise as a primary pitchfork bifurcation from the basic state at $b = 0$. From (3.18$b$) and (A 1$b$) this occurs at

$$\Omega^{1/2}R^{(\mathrm{e})} = R_{00}^{(\mathrm{c})} + \delta R_{01}^{(\mathrm{c})} + \epsilon^2\delta\left[-\left(\frac{2}{\pi}+\frac{\pi}{4}\right)\left(1+\Omega_{00}^{(\mathrm{c})}\right)\frac{\bar{\mathscr{C}}_{20}}{\bar{\mathscr{C}}_{00}^{(\mathrm{c})}}\right], \tag{4.2}$$

correct to $O(\delta)$ and $O(\epsilon^2)$, where $\bar{\mathscr{C}}_{20}$ can take either sign; see figure 2($b$,$c$). Note that the same result can be found from (3.1) in the present limit. Since the coefficient $c$ is always negative, the steady solutions exist for $b > 0$, or equivalently $R > R^{(\mathrm{e})}$, and are thus always supercritical. This is a consequence of the requirement that $K_1 = O(\delta)$ as $\delta \to 0$, as noted also by Anderson & Worster (1995).

The travelling waves are given by

$$|\mathscr{A}|^2 = -d/f, \quad \dot{\phi}_{\mathscr{A}}^2 = (-b + cd/f)/a \tag{4.3$a$,$b$}$$

and arise as a primary Hopf bifurcation from the basic state at $d = 0$, provided $b < 0$. From (3.18$d$) and (A 1$c$) this occurs at

$$\Omega^{1/2}R^{(\mathrm{o})} = R_{00}^{(\mathrm{c})} + \delta R_{01}^{(\mathrm{c})} + \epsilon^2\delta\left\{-\left(\frac{2}{\pi}+\frac{\pi}{4}\right)\left[1-\frac{12(\pi^2-8)}{(\pi^2+8)(\pi^2-9)}+\Omega_{00}^{(\mathrm{c})}\right]\frac{\bar{\mathscr{C}}_{20}}{\bar{\mathscr{C}}_{00}^{(\mathrm{c})}}\right\}, \tag{4.4}$$

provided $\bar{\mathscr{C}}_{20} < 0$ (so that $\bar{\mathscr{C}} < \bar{\mathscr{C}}^{(\mathrm{c})}$); see figure 2($b$). Again, the same result follows also from (3.1$a$) and (3.2) in the present limit. We observe that the coefficient $f$ is always negative so that the travelling waves exist for $d > 0$, or equivalently $R > R^{(\mathrm{o})}$, and are thus always supercritical, in agreement with results of Guba & Worster (2006).

The standing waves are characterized by an oscillation in the (real) amplitude. These solutions can be expressed in terms of Jacobian elliptic functions and analysed by the method of averaging (Dangelmayr & Knobloch 1987), a procedure used to study weakly dissipative nonlinear oscillators. In the present problem, they appear in two types. For $b(m - \frac{1}{2}) \geqslant 0$

$$\mathscr{A} = p\,\mathrm{cn}(q\tau|m), \quad \text{where} \quad p^2 = -\frac{2m}{2m-1}\frac{b}{c}, \quad q^2 = \frac{1}{2m-1}\frac{b}{a}, \tag{4.5$a$–$c$}$$

and the parameter $m$, $0 \leqslant m < 1$, satisfies

$$\frac{5cd}{2gb} = \frac{2(1-m+m^2)\Phi(m) - (1-m)(2-m)}{(2m-1)[1-m+(2m-1)\Phi(m)]}, \quad \Phi(m) \equiv \frac{\mathrm{E}(m)}{\mathrm{K}(m)}. \tag{4.6$a$,$b$}$$

Here $g = 2e + f$, and $\mathrm{K}(m)$ and $\mathrm{E}(m)$ are the complete elliptic integrals of the first and second kind, respectively. This solution represents a zero-mean oscillation about

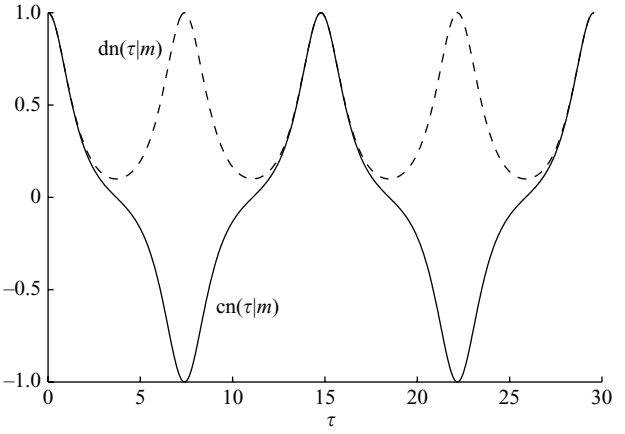


FIGURE 4. The functions $\mathrm{cn}(\tau|m)$ (solid) and $\mathrm{dn}(\tau|m)$ (dashed) valued for $m = 0.99$, illustrating the different possible dynamics of the nonlinear oscillatory solutions to (3.17). Note that the dnoidal oscillation has half the period of the cnoidal oscillation. As $m \to 0$, $\mathrm{cn}(\tau|m) \to \cos\tau$ and $\mathrm{dn}(\tau|m) \to 1$, but as $m$ increases the profiles acquire a characteristically spiky form as shown, resembling relaxation oscillations. As $m \to 1$, both profiles tend to sech $\tau$, with the periods becoming infinite.

the basic state (figure 4), with the period $4\mathrm{K}(m)(2m-1)^{1/2}(a/b)^{1/2}$. Equations (4.5) and (4.6) provide a parametric representation for the amplitude as a function of the Rayleigh number $R$. Note that for $m \to 0$ the solution becomes sinusoidal and $R \sim R^{(\mathrm{o})}$. Thus, these standing waves bifurcate simultaneously with the travelling waves at the primary Hopf bifurcation. The bifurcation is supercritical for $g < 0$ and subcritical otherwise (cf. Guba & Worster 2006).

For $b > 0$

$$\mathscr{A} = p\,\mathrm{dn}(q\tau|m), \quad \text{with} \quad p^2 = -\frac{2}{2-m}\frac{b}{c}, \quad q^2 = \frac{1}{2-m}\frac{b}{a}, \tag{4.7a–c}$$

where $m$ satisfies

$$\frac{5cd}{2gb} = \frac{(1-m)(2-m) - 2(1-m+m^2)\Phi(m)}{(2-m)[2(1-m) - (2-m)\Phi(m)]}. \tag{4.8}$$

This solution represents a non-zero-mean oscillation in amplitude about the steady state (4.1) (figure 4), with period $2\mathrm{K}(m)(2-m)^{1/2}(a/b)^{1/2}$. It arises as a secondary Hopf bifurcation from the steady-state solution branch; see § 4.2.

A further periodic solution, representing modulated waves, corresponds to travelling waves that are modulated as they drift. This solution arises as a secondary bifurcation from the branch of zero-mean standing waves. Further details can be found in Dangelmayr & Knobloch (1987, § 6). In the parameter regimes considered below, however, the modulated waves are in fact unstable.

### 4.2. *Bifurcation diagrams*

Recall that the quantities $c$ and $f$ are always negative, while $g$ can take either sign. Together with the existence and stability properties of solutions described in § 4.1, this implies that the $(\bar{S}, K_2)$-plane divides into nine regions, as shown in figure 5, each with different dynamics of (3.17). The predictions of the bifurcation analysis for these parameter regions are now discussed in turn.

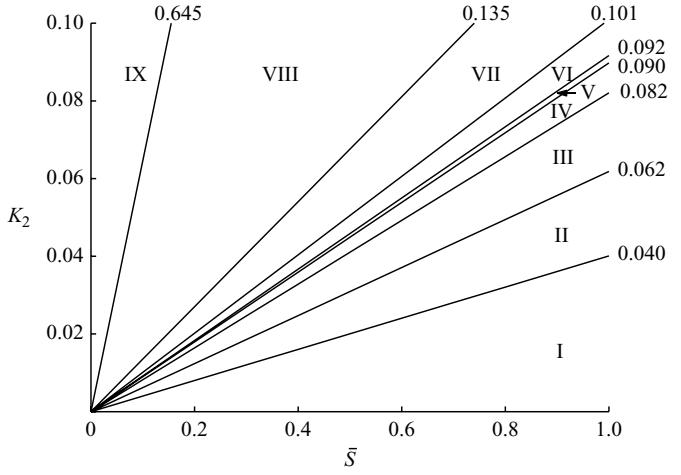


FIGURE 5. Parameter regimes in the $(\bar{S}, K_2)$-plane. The lines, marked by the slope $K_2/\bar{S}$, divide the plane into nine regions, labelled I–IX, each characterized by different dynamics of (3.17). The $O(\delta)$-corrections to boundaries between different regions have been ignored. The bifurcation diagrams corresponding to regions I, III, VIII and IX are shown in figure 6. Note that, for the oscillatory states, the diagram is appropriate for $1-\bar{\mathscr{C}}-(1-2\bar{\mathscr{C}})^{1/2} < \bar{S} < 1-\bar{\mathscr{C}}+(1-2\bar{\mathscr{C}})^{1/2}$ at fixed $\bar{\mathscr{C}}$, as inferred from (3.3*b*).

We first note that the coefficients $b$ and $d$ of the linear terms in (3.17) are related to the two independent bifurcation parameters, the Rayleigh number $R$ and the compositional ratio $\bar{\mathscr{C}}$. Figure 6 shows bifurcation diagrams for solutions of (3.17), describing the sequence of transitions as a distinguished bifurcation parameter, $R$, is increased, while keeping $\bar{\mathscr{C}}$ fixed. The bifurcation structures depend on whether $\bar{\mathscr{C}}$ is below or above its critical value $\bar{\mathscr{C}}^{(c)}$. With nine parameter regimes of figure 5, this makes for eighteen distinct cases in all. For illustration, we show in figure 6(*a–c*) the case when $\bar{\mathscr{C}} < \bar{\mathscr{C}}^{(c)}$, while in figure 6(*d*) the case when $\bar{\mathscr{C}} > \bar{\mathscr{C}}^{(c)}$.

The bifurcation diagram for region I of figure 5, given to leading order by

$$\frac{K_2}{\bar{S}} < \frac{6\pi^2(\pi^2-9)}{39\pi^4-151\pi^2-1024} \approx 0.040, \tag{4.9}$$

is displayed in figure 6(*a*). We observe that the primary Hopf bifurcation at $R^{(o)}$ gives rise to stable travelling waves and unstable zero-mean standing waves, both bifurcating supercritically. The travelling waves subsequently transfer stability to steady states in a secondary pitchfork bifurcation at $R = R^{(SS)}$, where

$$\Omega^{1/2}R^{(SS)} = R_{00}^{(c)} + \delta R_{01}^{(c)} + \epsilon^2\delta\left\{-\left(\frac{2}{\pi}+\frac{\pi}{4}\right) \times \left[\frac{(\pi^4-13\pi^2+24)c-3(\pi^4-64)f}{(\pi^2+8)[(\pi^2-9)c-3(\pi^2-8)f]} + \Omega_{00}^{(c)}\right]\frac{\bar{\mathscr{C}}_{20}}{\bar{\mathscr{C}}_{00}^{(c)}}\right\}. \tag{4.10}$$

The zero-mean standing-wave branch develops a turning point, followed by the smooth transition at infinite period to a branch of non-zero-mean standing waves. Note that both standing-wave branches are completely unstable. Also, note that the stable oscillatory solution, the travelling waves, is the one with the larger Nusselt number (proportional to $|\mathscr{A}|^2$), thus advecting more heat and solute across the system.

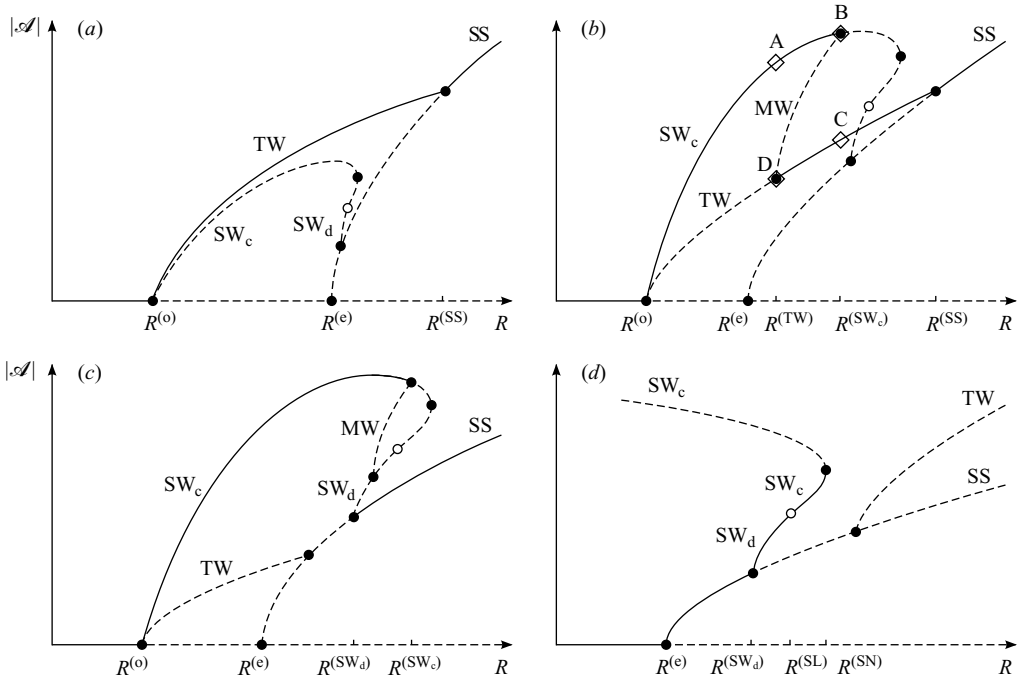


FIGURE 6. Bifurcation diagrams. The sketches show the bifurcation sequences as $R$ is increased with fixed $\bar{\mathscr{C}}$ for (*a*) region I, (*b*) region III, (*c*) region VIII and (*d*) region IX of figure 5. For steady states $|\mathscr{A}|$ is shown, while for oscillatory states the root-mean-square value of $|\mathscr{A}|$ is indicated. The labels SS, TW, $\mathrm{SW_c}$, $\mathrm{SW_d}$ and MW denote steady states, travelling waves, cnoidal standing waves, dnoidal standing waves and modulated waves, respectively. Solid (dashed) curves represent stable (unstable) solution branches. Filled (open) circles represent local (global) bifurcations. In (*a–c*) $\bar{\mathscr{C}} < \bar{\mathscr{C}}^{(\mathrm{c})}$, while in (*d*) $\bar{\mathscr{C}} > \bar{\mathscr{C}}^{(\mathrm{c})}$. The basic-state solution loses stability to steady states at $R^{(\mathrm{e})}$ and to oscillatory states at $R^{(\mathrm{o})}$. Note that no primary Hopf bifurcation occurs in (*d*). Also indicated are the Rayleigh numbers $R^{(\mathrm{SS})}$, $R^{(\mathrm{TW})}$, $R^{(\mathrm{SW_c})}$, $R^{(\mathrm{SW_d})}$, $R^{(\mathrm{SL})}$ and $R^{(\mathrm{SN})}$ of the secondary bifurcation points at which the stability exchanges take place. Note the regions of multiple stable states in (*b*) and (*c*). The path ABCDA, indicated in (*b*), constitutes a hysteresis loop.

Region II of figure 5 is given to leading order by

$$0.040 < \frac{K_2}{\bar{S}} < \frac{6\pi^2(\pi^2-9)}{21\pi^4-71\pi^2-512} \approx 0.062. \tag{4.11}$$

In this case, the bifurcation structure is similar to that for region I, except that the initial instability is to stable standing waves rather than to travelling waves, which subsequently transfer stability to travelling waves via an intermediate branch of modulated waves.

Region III of figure 5 is given to leading order by

$$0.062 < \frac{K_2}{\bar{S}} < \frac{6\pi^2(\pi^2-9)(3\tilde{c}_1-1)}{(1024+187\pi^2-27\pi^4)\tilde{c}_1-1024-169\pi^2+33\pi^4} \approx 0.082, \tag{4.12}$$

where $\tilde{c}_1 \approx 0.70$. As shown in figure 6(*b*), this case exhibits a range of Rayleigh numbers where both the zero-mean standing waves and the travelling waves are stable. Analysing the structure and stability of these solutions, we find that this

bistability region extends from $R^{(\mathrm{TW})}$ to $R^{(\mathrm{SW_c})}$, where

$$\Omega^{1/2}R^{(\mathrm{TW})} = R_{00}^{(\mathrm{c})} + \delta R_{01}^{(\mathrm{c})} + \epsilon^2\delta\left\{-\left(\frac{2}{\pi}+\frac{\pi}{4}\right)\right.$$
$$\left.\times\left[\frac{(\pi^4-13\pi^2+24)(3g-5f)c-6(\pi^4-64)(g-2f)f}{(\pi^2+8)[(\pi^2-9)(3g-5f)c-6(\pi^2-8)(g-2f)f]}+\Omega_{00}^{(\mathrm{c})}\right]\frac{\bar{\mathscr{C}}_{20}}{\bar{\mathscr{C}}_{00}^{(\mathrm{c})}}\right\}, \quad (4.13a)$$

$$\Omega^{1/2}R^{(\mathrm{SW_c})} = R_{00}^{(\mathrm{c})} + \delta R_{01}^{(\mathrm{c})} + \epsilon^2\delta\left\{-\left(\frac{2}{\pi}+\frac{\pi}{4}\right)\right.$$
$$\left.\times\left[\frac{(\pi^4-13\pi^2+24)(2m-1)c-6(\pi^4-64)[\Phi(m)+m-1]f}{(\pi^2+8)\{(\pi^2-9)(2m-1)c-6(\pi^2-8)[\Phi(m)+m-1]f\}}+\Omega_{00}^{(\mathrm{c})}\right]\frac{\bar{\mathscr{C}}_{20}}{\bar{\mathscr{C}}_{00}^{(\mathrm{c})}}\right\} \quad (4.13b)$$

and $m$ satisfies

$$\frac{f}{g} = \frac{2(1-m+m^2)\Phi(m)-(1-m)(2-m)}{5\,[\Phi(m)+m-1]\,[1-m+(2m-1)\,\Phi(m)]}. \quad (4.14)$$

As $R$ increases, a path AB along the stable portion of the standing-wave branch, shown in figure 6($b$), results in a jump down to stable travelling waves at point C. If $R$ is increased further, travelling-wave convection persists. However, if $R$ is decreased along CD then there is a jump up to standing waves. Thus, the path ABCDA constitutes a hysteresis loop.

The parameter regimes for regions IV–VII of figure 5 are given to leading order by

$$0.082 < \frac{K_2}{\bar{S}} < \frac{6\pi^2(\pi^2-9)(3\tilde{c}_2-1)}{(1024+187\pi^2-27\pi^4)\tilde{c}_2-1024-169\pi^2+33\pi^4} \approx 0.090, \quad (4.15a)$$

$$0.090 < \frac{K_2}{\bar{S}} < \frac{30\pi^2(\pi^2-9)}{51\pi^4-115\pi^2-1024} \approx 0.092, \quad (4.15b)$$

$$0.092 < \frac{K_2}{\bar{S}} < \frac{42\pi^2(\pi^2-9)}{57\pi^4-97\pi^2-1024} \approx 0.101, \quad (4.15c)$$

$$0.101 < \frac{K_2}{\bar{S}} < \frac{2(\pi^2-9)}{\pi^2+3} \approx 0.135, \quad (4.15d)$$

respectively, where $\tilde{c}_2 \approx 0.74$. The associated bifurcation structures are found to differ from that for region III in the relative positions of the secondary bifurcation points, but not in the nature of the stable solution branches, and thus have been omitted from figure 6.

In figure 6($c$), we show the bifurcation diagram appropriate for region VIII of figure 5, where

$$0.135 < \frac{K_2}{\bar{S}} < \frac{18\pi^2(\pi^2-9)}{1024+187\pi^2-27\pi^4} \approx 0.645, \quad (4.16)$$

with corrections at $O(\delta)$. Again, as in figure 6($b$), there is a region of bistability accompanied by discontinuous transitions, but now involving jump transitions between zero-mean standing waves and steady states. This bistability region extends from $R^{(\mathrm{SW_d})}$ to $R^{(\mathrm{SW_c})}$, where $R^{(\mathrm{SW_d})}$ is given by (4.10) with $f$ replaced by $g$.

Finally, in figure 6($d$) we show the bifurcation structure for region IX of figure 5, where

$$\frac{K_2}{\bar{S}} > 0.645, \quad (4.17)$$

with corrections at $O(\delta)$. Note that we consider $\bar{\mathscr{C}} > \bar{\mathscr{C}}^{(c)}$ here, so there is no primary Hopf bifurcation. The notable feature of this graph is a branch of stable non-zero-mean standing waves, bifurcating off the steady branch in a secondary Hopf bifurcation at $R^{(SW_d)}$. Solutions on this branch correspond to vacillations about the steady state without flow reversal, similar to the periodic behaviour seen by Peppin *et al.* (2008). As $R$ increases, these periodic solutions are superseded by the stable zero-mean standing waves at $R^{(SL)}$, where

$$\Omega^{1/2}R^{(SL)} = R_{00}^{(c)} + \delta R_{01}^{(c)} + \epsilon^2\delta\left\{-\left(\frac{2}{\pi}+\frac{\pi}{4}\right)\right.$$
$$\left.\times\left[\frac{5(\pi^4-13\pi^2+24)c-12(\pi^4-64)g}{(\pi^2+8)[5(\pi^2-9)c-12(\pi^2-8)g]}+\Omega_{00}^{(c)}\right]\frac{\bar{\mathscr{C}}_{20}}{\bar{\mathscr{C}}_{00}^{(c)}}\right\}. \quad (4.18)$$

This oscillatory branch continues up to $R^{(SN)}$, given by (4.13*b*) with $f$ replaced by $g$, where it loses stability in a saddle-node bifurcation. To investigate the eventual stabilization of the zero-mean standing waves at higher amplitudes would require a higher-order calculation, which is outside the scope of the present theory.

It is worth pointing out that the existence of all the bifurcation structures of figure 6 is controlled only by the parameter combination $K_2/\delta S$. Physically, this term represents higher-order nonuniformity of the permeability due to the basic-state solid fraction and its perturbations. Neither of these bifurcation scenarios would have been identified had we assumed uniform permeability of the mushy layer, or had we chosen $S = O(1)$ rather than the distinguished limit $S/\mathscr{C} = O(1)$.

### 4.3. *Stability maps: physical considerations*

The foregoing analysis has highlighted the roles played by the secondary bifurcations in determining the stable convection patterns at fixed compositional ratio $\bar{\mathscr{C}}$. The Rayleigh numbers corresponding to the secondary bifurcation points depend in a complicated way on the control parameters of the system. We now examine the effect of varying $\bar{\mathscr{C}}$ and, by doing so, identify the stable parameter regimes for convective flows in mushy layers.

The nonlinear-stability results in the $(\bar{\mathscr{C}}, R)$-plane are summarized in figure 7. Four representative sets of parameter values have been chosen so that the predictions shown in figure 7(*a–d*) correspond respectively to regimes I, III, VIII and IX identified in figure 5. The curves indicate the paths of the primary $\left(R^{(e)}, R^{(o)}\right)$ and secondary $\left(R^{(SS)}, R^{(TW)}, R^{(SW_c)}, R^{(SW_d)}, R^{(SL)}, R^{(SN)}\right)$ bifurcation points, separating the plane into regions with different stable convection patterns. In each plot, the paths not involved in the stability exchanges have been omitted. In figure 7(*a–c*) varying $R$ corresponds to a slice through $\bar{\mathscr{C}} < \bar{\mathscr{C}}^{(c)}$ in figure 6(*a–c*); similarly, between figure 7(*d*) and $\bar{\mathscr{C}} > \bar{\mathscr{C}}^{(c)}$ in figure 6(*d*). In figure 7(*d*), the paths $R^{(SL)}$ and $R^{(SN)}$ (not indicated) nearly overlap with the path $R^{(SW_d)}$, and so the regions of stable zero-mean and non-zero-mean standing waves are not discernible.

In an experiment involving a specific alloy, there are two degrees of freedom: the pulling speed $V$ and the initial composition $C_0$. Note that increasing $V$ is not expected to affect the dimensionless mushy-layer thickness $\delta = d/(\kappa/V)$, because the dimensional depth of the layer will vary as $d \propto 1/V$. Since the two control parameters $V$ and $C_0$ are merged into $R$, and $C_0$ is involved in both $\bar{S}$ and $\bar{\mathscr{C}}$, the results of figure 7 cannot be easily applied to the physically relevant situation of $C_0$ fixed as $V$ increases, or vice versa. This difficulty can be overcome by returning to dimensional

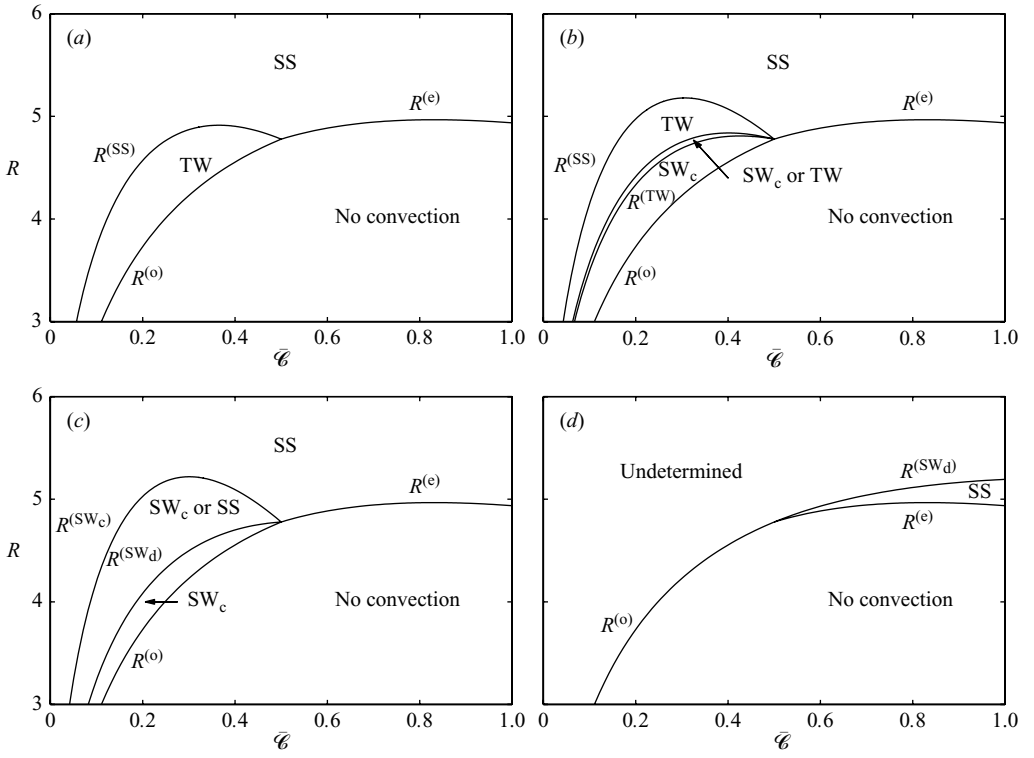


FIGURE 7. Stability maps. The paths of the primary ($R^{(e)}$, $R^{(o)}$) and secondary ($R^{(SS)}$, $R^{(TW)}$, $R^{(SW_c)}$, $R^{(SW_d)}$, $R^{(SL)}$, $R^{(SN)}$) bifurcation points in the $(\bar{\mathscr{C}}, R)$-plane shown for representative cases (*a*) $K_2 = 0.005$, (*b*) $K_2 = 0.06$, (*c*) $K_2 = 0.1$ and (*d*) $K_2 = 1$, with $\bar{S} = 0.5$, $\bar{K}_1 = 0.06$, $K_3 = 0$ and $\delta = 0.2$. The results in (*a–d*) correspond to the parameter regimes I, III, VIII and IX of figure 5, respectively. In each case, all the bifurcation paths meet at the point $(\bar{\mathscr{C}}^{(c)}, R^{(c)}) \approx (0.5, 4.8)$. The different regions are labelled by the stable pattern predicted therein. The labels have the same significance as in figure 6. Note the regions of multiple stable states in (*b*) and (*c*). In (*d*), the paths $R^{(SL)}$ and $R^{(SN)}$ are not resolved on the scale of the figure but lie just above the curve $R^{(SW_d)}$ for $\bar{\mathscr{C}} > \bar{\mathscr{C}}^{(c)}$.

variables. As an illustrative example, we specialize our results so that they apply to a particular binary alloy, the ammonium chloride–water system. Using relevant values for material parameters (e.g. Emms & Fowler 1994, and references therein), we show in figure 8 a regime diagram for this system, indicating the domains of stability in terms of the pulling speed $V$ and the initial composition $C_0$. The other (dimensionless) parameters have been chosen as $\bar{K}_1 = 0.5$, $K_2 = 0.08$, $K_3 = 0$ and $\delta = 0.02$, so that the results shown correspond to regime VIII in figure 5.

In an experiment in which $C_0$ is fixed and $V$ is increased from zero, figure 8 can be used to predict transitions. Note, in particular, that the regions of stable steady states and zero-mean standing waves are separated by a region in which the two types of states coexist. This bistability region is accompanied by a dynamical hysteresis behaviour (cf. figure 6*c*). Specifically, as $V$ increases, there is a snap-through transition from the steady states to standing-wave convection, occurring along the curve bounding the bistability region on its right. If $V$ is then decreased, however, a jump back to the steady states would occur at much lower values of $V$ as determined

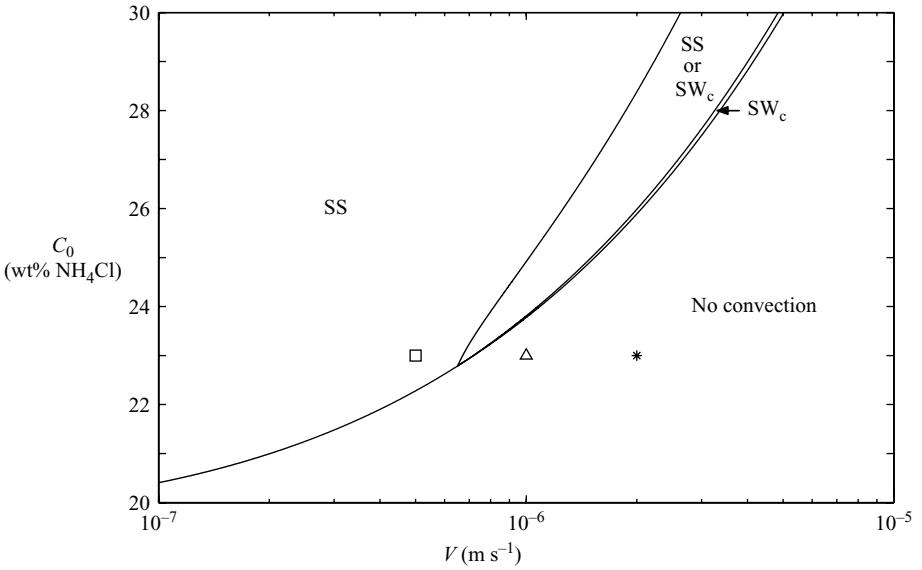


FIGURE 8. Regime diagram. The diagram quantifies the operating conditions in the $(V, C_0)$-plane at which different stable convective flows are predicted. The labels have the same significance as in figure 6. The material parameters used are appropriate for $NH_4Cl$–$H_2O$ systems. The other parameter values are adjusted so that the results shown correspond to regime VIII in figure 5. The data are taken from experiments by Peppin *et al.* (2008), indicating different solidification regimes observed: a mushy layer with steady-state chimney convection, □; a mushy layer with oscillatory chimney convection (a 'breathing mode'), △; and a mushy layer with no chimneys, ∗.

by the curve bounding the bistability region on its left. Also indicated are the data points taken from Peppin *et al.* (2008), with the square corresponding to the observed steady-state chimney convection, the triangle corresponding to the oscillatory chimney convection and the asterisk corresponding to a mushy layer with no chimneys. It must be borne in mind that the present theory pertains to nonlinear convection in mushy layers without the formation of chimneys, whereas the experimentally observed convecting states feature fully developed chimneys. Nevertheless, the theory and experiments are consistent in showing the transition from steadily convecting states to non-convecting states through an intermediate regime of oscillatory convective behaviour.

## 5. Conclusions

We have examined the nonlinear stability of convection in a mushy layer during binary alloy solidification. Based on a model of the mushy layer given by Amberg & Homsy (1993), our analysis extends the linear (Anderson & Worster 1996) and weakly nonlinear (Anderson & Worster 1995; Guba & Worster 2006) stability analyses by considering a regime in which steady convection interacts with oscillatory convection at finite amplitude. In this regime, the Rayleigh number for the onset of oscillatory convection differs from that for the onset of steady convection by only a small amount, and the oscillation frequency is small. An appropriate scaling allows us to carry out the nonlinear analysis analytically. A pivotal result of our analysis is a complex amplitude equation (3.17), which describes the dynamics of the system

near the simultaneous onset of steady and oscillatory convection. An analysis of this equation reveals a number of interesting results concerning nonlinear convection in mushy layers.

We have identified the three primary solution branches that bifurcate from the basic state: steady states, travelling waves and zero-mean standing waves. In the parameter regime considered, namely that in which $K_1/\bar{\mathscr{C}} = O(\delta)$, both primary oscillatory branches bifurcate supercritically, and the stable solution is the one with larger amplitude. We have analysed the stability of each solution and identified a number of secondary bifurcations. The secondary bifurcations play an important role in the stability exchanges that take place as the Rayleigh number varies at fixed compositional ratio. A variety of possible bifurcation scenarios are summarized in the bifurcation diagrams of § 4.2. We find that, at a given compositional ratio, the prediction of a type of bifurcation structure hinges upon a single physical effect associated with higher-order permeability variations owing to the basic-state solid fraction and its perturbations. It is the nonlinear interaction between solid fraction and temperature field that controls the bifurcation structure in the present mushy-layer system.

We have also identified new stability limits associated with the modal stability exchanges at the secondary bifurcation points. We have determined how these nonlinear stability limits vary with the compositional ratio of the binary mixture. Comprehensive stability maps have been obtained which show the alternative stable convection patterns expected for particular operating conditions and illustrate most clearly their non-unique nature. Our analytical predictions capture qualitatively some of the features of mushy-layer convection observed experimentally by Peppin *et al.* (2008).

We point out that the present analysis is valid for a single, externally imposed wavenumber, $k = \pi$. Although this value does minimize the Rayleigh number for the onset of the steady mode of instability, the preferred wavenumber for the oscillatory mode is always greater in the available parameter space. Said another way, the steady and oscillatory modes cannot be simultaneously critical at the same wavenumber. Nevertheless, we expect the analysis to be particularly relevant to situations where experimental control can be enforced on the size of convection cells.

We note that we have considered a particular parameter regime, namely that in which $K_1/\bar{\mathscr{C}} = O(\delta)$, so that the bifurcation to steady-state convection is always supercritical. When $K_1/\bar{\mathscr{C}} = O(1)$, the bifurcation to steady-state convection may be subcritical (Amberg & Homsy 1993). Together with the sub- or supercritically bifurcating oscillatory branches (Guba & Worster 2006), this may have important ramifications in terms of branching behaviour and nonlinear stability.

The present study is based on a mushy-layer model that, employing a rigid-lid approximation, eliminates any interaction between the mushy and liquid regions (Amberg & Homsy 1993). Recently, some efforts have been made to relax the impermeability (Chung & Chen 2000), and both the impermeability and rigidity (Roper *et al.* 2008) of the mush–liquid interface. While certainly more realistic, these generalizations showed, in particular, that the important qualitative results, such as the topology of neutral stability curves and parametric trends in terms of nonlinear stability criteria, were preserved, though at slightly modified parameter values. We expect the qualitative essence of a mode interaction between steady and oscillatory convection, elucidated in the present paper, to be robust to similar model generalizations.

The numerous bifurcation features already apparent in the linear theory may lead to an even richer variety of structures when nonlinear regimes are considered. For example, the critical wavenumber separation noted above is particularly interesting, as it points to another codimension-two bifurcation problem with similarly varied dynamics. Recent studies of pattern-forming systems with competing instabilities (Porter & Knobloch 2001; Dawes & Proctor 2008) lend support to this view. In the present system, the ensuing finite-amplitude motion would be a larger scale steady convective flow with a smaller scale oscillatory wave riding on it. A detailed investigation of this possibility remains an open issue.

The authors would like to thank D. M. Anderson for helpful comments on a draft of this paper and J. H. P. Dawes, M. A. Hallworth and S. S. L. Peppin for helpful discussions. This study has been supported in part by the Engineering and Physical Sciences Research Council under grant EP/F036701/1 (P.G. and M.G.W.) and the Research and Development Agency under grants ESF-EC-0206 and APVV-0247-06 (P.G.).

## Appendix. Coefficients in the amplitude equation

The coefficients $\bar{a}_1$, $b_1$ and $d_1$ of the linear terms in (3.17) have the forms

$$\begin{aligned}\bar{a}_1 = {} & \left(-\frac{1}{8}+\frac{8}{\pi^4}-\frac{17(\pi^2-8)}{16\sqrt{3}\pi^3}\coth\sqrt{3}\pi-\frac{\pi^2-8}{16\sqrt{3}\pi^3}\operatorname{csch}\sqrt{3}\pi\right)\Omega_{00}^{(c)2}\\ & +\left(-\frac{1}{8}+\frac{56}{3\pi^4}-\frac{37}{18\pi^2}+\frac{254-27\pi^2}{36\sqrt{3}\pi^3}\coth\sqrt{3}\pi-\frac{2+51\pi^2}{36\sqrt{3}\pi^3}\operatorname{csch}\sqrt{3}\pi\right)\frac{1}{\bar{\mathscr{C}}_{00}^{(c)}}\\ & +\left(\frac{41}{24}+\frac{136}{\pi^4}-\frac{521}{18\pi^2}+\frac{21\pi^2-206}{36\sqrt{3}\pi^3}\coth\sqrt{3}\pi+\frac{93\pi^2-334}{36\sqrt{3}\pi^3}\operatorname{csch}\sqrt{3}\pi\right)\frac{\Omega_{00}^{(c)}}{\bar{\mathscr{C}}_{00}^{(c)}}\\ & +\left(-\frac{7}{12}-\frac{80}{3\pi^4}+\frac{8}{\pi^2}+\frac{\pi^2-8}{6\sqrt{3}\pi^3}\coth\sqrt{3}\pi-\frac{7(\pi^2-8)}{6\sqrt{3}\pi^3}\operatorname{csch}\sqrt{3}\pi\right)\frac{\Omega_{00}^{(c)2}}{\bar{\mathscr{C}}_{00}^{(c)}}, \quad (A\,1a)\end{aligned}$$

$$b_1 = 2\pi R_{21}+\left(4+\frac{\pi^2}{2}\right)\left(1+\Omega_{00}^{(c)}\right)\frac{\bar{\mathscr{C}}_{20}}{\bar{\mathscr{C}}_{00}^{(c)}}, \quad (A\,1b)$$

$$d_1 = \frac{2\pi(\pi^2-9)}{3(\pi^2-8)}R_{21}+\left(\frac{24-13\pi^2+\pi^4}{6(\pi^2-8)}+\frac{(\pi^2+8)(\pi^2-9)}{6(\pi^2-8)}\Omega_{00}^{(c)}\right)\frac{\bar{\mathscr{C}}_{20}}{\bar{\mathscr{C}}_{00}^{(c)}}. \quad (A\,1c)$$

The coefficients $c_1$, $e_1$ and $f_1$ of the cubic terms in (3.17) have the forms

$$\begin{aligned}c_1 = {} & 4\pi^4\frac{\bar{K}_1}{\Omega_{00}^{(c)}\bar{\mathscr{C}}_{00}^{(c)}}-\left(\frac{416\pi^2}{3}+33\pi^4\right)\frac{K_3}{\Omega_{00}^{(c)2}\bar{\mathscr{C}}_{00}^{(c)3}}+\left(\frac{4000\pi^2}{9}-44\pi^4\right)\frac{K_2}{\Omega_{00}^{(c)2}\bar{\mathscr{C}}_{00}^{(c)3}}\\ & -\left(\frac{56962\pi^2}{189}-\frac{217\pi^4}{6}-\frac{11\sqrt{3}\pi^3}{4}\coth\frac{\sqrt{3}\pi}{2}-\frac{65\pi^3}{3\sqrt{3}}\coth\sqrt{3}\pi\right.\\ & \left.+\frac{11\pi^3}{3\sqrt{3}}\operatorname{csch}\sqrt{3}\pi\right)\frac{K_2}{\Omega_{00}^{(c)}\bar{\mathscr{C}}_{00}^{(c)2}}-\left(\frac{40\pi^2}{9}-\frac{\sqrt{3}\pi^3}{4}\coth\frac{\sqrt{3}\pi}{2}-\frac{2\pi^3}{\sqrt{3}}\tanh\frac{\sqrt{3}\pi}{2}\right)\Omega_{00}^{(c)}, \quad (A\,2a)\end{aligned}$$

$$e_1 = -\frac{2\pi^4(\pi^2-6)}{3(\pi^2-8)}\frac{\bar{K}_1}{\Omega_{00}^{(c)}\bar{\mathscr{C}}_{00}^{(c)}} + \left(\frac{1208}{9} + \frac{7\pi^2}{9} + 5\pi^4 + \frac{9664}{9(\pi^2-8)}\right)\frac{K_3}{\Omega_{00}^{(c)2}\bar{\mathscr{C}}_{00}^{(c)3}}$$
$$- \left(\frac{832}{27} - \frac{292\pi^2}{27} + \frac{4\pi^4}{3} + \frac{6656}{27(\pi^2-8)}\right)\frac{K_2}{\Omega_{00}^{(c)2}\bar{\mathscr{C}}_{00}^{(c)3}}$$
$$+ \left[\frac{18406}{567} - \frac{37561\pi^2}{2268} - \frac{2\pi^4}{3} + \frac{18224}{567(\pi^2-8)}\right.$$
$$- \left(\frac{19\pi}{4\sqrt{3}} - \frac{11\pi^3}{4\sqrt{3}} + \frac{22\pi}{\sqrt{3}(\pi^2-8)}\right)\coth\frac{\sqrt{3}\pi}{2}$$
$$\left. - \frac{\pi^3(173\pi^2-1254)}{18\sqrt{3}(\pi^2-8)}\coth\sqrt{3}\pi + \frac{\pi^3(59\pi^2-450)}{18\sqrt{3}(\pi^2-8)}\operatorname{csch}\sqrt{3}\pi\right]\frac{K_2}{\Omega_{00}^{(c)}\bar{\mathscr{C}}_{00}^{(c)2}}$$
$$- \left(\frac{10\pi^2(\pi^2-12)}{27(\pi^2-8)} - \frac{\pi^3(\pi^2-9)}{4\sqrt{3}(\pi^2-8)}\coth\frac{\sqrt{3}\pi}{2} - \frac{2\pi^3(\pi^2-9)}{3\sqrt{3}(\pi^2-8)}\tanh\frac{\sqrt{3}\pi}{2}\right)\Omega_{00}^{(c)}, \tag{A 2b}$$

$$f_1 = \frac{4\pi^4(\pi^2-9)}{3(\pi^2-8)}\frac{\bar{K}_1}{\Omega_{00}^{(c)}\bar{\mathscr{C}}_{00}^{(c)}} + \left(\frac{1208}{9} - \frac{1130\pi^2}{9} - 11\pi^4 + \frac{9664}{9(\pi^2-8)}\right)\frac{K_3}{\Omega_{00}^{(c)2}\bar{\mathscr{C}}_{00}^{(c)3}}$$
$$+ \left(\frac{11456}{27} + \frac{3718\pi^2}{27} - \frac{44\pi^4}{3} - \frac{6656}{27(\pi^2-8)}\right)\frac{K_2}{\Omega_{00}^{(c)2}\bar{\mathscr{C}}_{00}^{(c)3}}$$
$$- \left[\frac{107930}{567} + \frac{108593\pi^2}{1134} - \frac{211\pi^4}{18} - \frac{18224}{567(\pi^2-8)}\right.$$
$$+ \left(\frac{3\pi}{4\sqrt{3}} - \frac{11\pi^3}{4\sqrt{3}} + \frac{22\pi}{\sqrt{3}(\pi^2-8)}\right)\coth\frac{\sqrt{3}\pi}{2}$$
$$- \left(\frac{8654\pi}{147\sqrt{3}} + \frac{65\pi^3}{9\sqrt{3}} - \frac{520\pi}{9\sqrt{3}(\pi^2-8)}\right)\coth\sqrt{3}\pi$$
$$\left. - \left(\frac{3830\pi}{441\sqrt{3}} - \frac{11\pi^3}{9\sqrt{3}} + \frac{88\pi}{9\sqrt{3}(\pi^2-8)}\right)\operatorname{csch}\sqrt{3}\pi\right]\frac{K_2}{\Omega_{00}^{(c)}\bar{\mathscr{C}}_{00}^{(c)2}}$$
$$- \left(\frac{10\pi^2(7\pi^2-60)}{27(\pi^2-8)} - \frac{\pi^3(\pi^2-9)}{4\sqrt{3}(\pi^2-8)}\coth\frac{\sqrt{3}\pi}{2} - \frac{2\pi^3(\pi^2-9)}{3\sqrt{3}(\pi^2-8)}\tanh\frac{\sqrt{3}\pi}{2}\right)\Omega_{00}^{(c)}. \tag{A 2c}$$

The expression for $\bar{\mathscr{C}}_{01}^{(c)}$, appearing in the $O(\delta^1)$ correction term to the critical compositional ratio in (3.3*b*), has the form

$$\bar{\mathscr{C}}_{01}^{(c)} = -\frac{25}{12} + \frac{34}{3\pi^2} + \frac{\coth\sqrt{3}\pi}{6\sqrt{3}\pi} - \frac{7\operatorname{csch}\sqrt{3}\pi}{6\sqrt{3}\pi} + \left(\frac{7}{12} - \frac{10}{3\pi^2} - \frac{\coth\sqrt{3}\pi}{6\sqrt{3}\pi} + \frac{7\operatorname{csch}\sqrt{3}\pi}{6\sqrt{3}\pi}\right)\Omega_{00}^{(c)}. \tag{A 3}$$

It is worth pointing out that the same expression can be obtained by setting the coefficient $a_1$ in (A 1*a*) of Anderson & Worster (1995), approximated correct to $O(\epsilon^0\delta^1)$ in the present limit, to zero, providing a further check of our results.

## REFERENCES

Amberg, G. & Homsy, G. M. 1993 Nonlinear analysis of buoyant convection in binary solidification with application to channel formation. *J. Fluid Mech.* **252**, 79–98.

Anderson, D. M. & Worster, M. G. 1995 Weakly nonlinear analysis of convection in mushy layers during the solidification of binary alloys. *J. Fluid Mech.* **302**, 307–331.

Anderson, D. M. & Worster, M. G. 1996 A new oscillatory instability in a mushy layer during the solidification of binary alloys. *J. Fluid Mech.* **307**, 245–267.

Chung, C. A. & Chen, F. 2000 Onset of plume convection in mushy layers. *J. Fluid Mech.* **408**, 53–82.

Chung, C. A. & Worster, M. G. 2002 Steady-state chimneys in a mushy layer. *J. Fluid Mech.* **455**, 387–411.

Copley, S. M., Giamei, A. F., Johnson, S. M. & Hornbecker, M. F. 1970 The origin of freckles in unidirectionally solidified castings. *Metall. Trans.* **1**, 2193–2204.

Coullet, P. H. & Spiegel, E. A. 1983 Amplitude equations for systems with competing instabilities. *SIAM J. Appl. Math.* **43**, 776–821.

Dangelmayr, G. & Knobloch, E. 1986 Interaction between standing and travelling waves and steady states in magnetoconvection. *Phys. Lett.* A **117**, 394–398.

Dangelmayr, G. & Knobloch, E. 1987 The Takens–Bogdanov bifurcation with O(2)-symmetry. *Phil. Trans. R. Soc. Lond.* A **322**, 243–279.

Davis, S. H. 2001 *Theory of Solidification*. Cambridge University Press.

Dawes, J. H. P. & Proctor, M. R. E. 2008 Secondary Turing-type instabilities due to strong spatial resonance. *Proc. Roy. Soc. Lond.* A **464**, 923–942.

Emms, P. W. & Fowler, A. C. 1994 Compositional convection in the solidification of binary alloys. *J. Fluid Mech.* **262**, 111–139.

Fowler, A. C. 1985 The formation of freckles in binary alloys. *IMA J. Appl. Maths.* **35**, 159–174.

Guba, P. & Worster, M. G. 2006 Nonlinear oscillatory convection in mushy layers. *J. Fluid Mech.* **553**, 419–443.

Guckenheimer, J. & Knobloch, E. 1983 Nonlinear convection in a rotating layer: amplitude expansions and normal forms. *Geophys. Astrophys. Fluid Dyn.* **23**, 247–272.

Knobloch, E. 1986 Oscillatory convection in binary mixtures. *Phys. Rev.* A **34**, 1538–1549.

Knobloch, E. & Proctor, M. R. E. 1981 Nonlinear periodic convection in double-diffusive systems. *J. Fluid Mech.* **108**, 291–316.

Knobloch, E. & Silber, M. 1990 Travelling wave convection in a rotating layer. *Geophys. Astrophys. Fluid Dyn.* **51**, 195–209.

Palm, E., Weber, J. E. & Kvernvold, O. 1972 On steady convection in a porous medium. *J. Fluid Mech.* **54**, 153–161.

Peppin, S. S. L., Huppert, H. E. & Worster, M. G. 2008 Steady-state solidification of aqueous ammonium chloride. *J. Fluid Mech.* **599**, 465–476.

Porter, J. & Knobloch, E. 2001 New type of complex dynamics in the 1:2 spatial resonance. *Physica* D **159**, 125–154.

Riahi, D. N. 2002 On nonlinear convection in mushy layers. Part 1. Oscillatory modes of convection. *J. Fluid Mech.* **467**, 331–359.

Riahi, D. N. 2004 On nonlinear convection in mushy layers. Part 2. Mixed oscillatory and stationary modes of convection. *J. Fluid Mech.* **517**, 71–102.

Roper, S. M., Davis, S. H. & Voorhees, P. W. 2008 An analysis of convection in a mushy layer with a deformable permeable interface. *J. Fluid Mech.* **596**, 333–352.

Rucklidge, A. M., Weiss, N. O., Brownjohn, D. P. & Proctor, M. R. E. 1993 Oscillations and secondary bifurcations in nonlinear magnetoconvection. *Geophys. Astrophys. Fluid Dyn.* **68**, 133–150.

Schulze, T. P. & Worster, M. G. 1998 A numerical investigation of steady convection in mushy layers during the directional solidification of binary alloys. *J. Fluid Mech.* **356**, 199–220.

Schulze, T. P. & Worster, M. G. 1999 Weak convection, liquid inclusions and the formation of chimneys in mushy layers. *J. Fluid Mech.* **388**, 197–215.

Solomon, T. H. & Hartley, R. R. 1998 Measurements of the temperature field of mushy and liquid regions during solidification of aqueous ammonium chloride. *J. Fluid Mech.* **358**, 87–106.

Spiegel, E. A. 1994 Physics of convection. In *Lecture Notes, Workshop on Fluid Mechanics, Trieste*, pp. 43–54.

Worster, M. G. 1992 Instabilities of the liquid and mushy regions during solidification of alloys. *J. Fluid Mech.* **237**, 649–669.

Worster, M. G. 1997 Convection in mushy layers. *Annu. Rev. Fluid Mech.* **29**, 91–122.

Worster, M. G. 2000 Solidification of fluids. In *Perspectives in Fluid Dynamics* (ed. G. K. Batchelor, H. K. Moffatt & M. G. Worster), pp. 393–446. Cambridge University Press.